Dalton Transactions

PAPER

Check for updates

Volatile lanthanide complexes with fluorinated heptadentate ligands†

Joshua C. Zgrabik,[a] Balaka Bhuniya,[a] Thomas Branstad Phillips,[a] Jorge Barroso, [b] [b] Bess Vlaisavljevich [b] [b] and Scott R. Daly [b] *[a]

Understanding factors that influence the volatility of lanthanide complexes remains an important goal for applications such as gas-phase f-metal separations and the synthesis of lanthanide-containing thin films. Lanthanide complexes often exhibit volatility differences that depend on the ability of ligands to saturate the lanthanide coordination sphere and attenuate intermolecular bonding in the solid state. This can make it difficult to assess how electronic factors associated with differing ligand substituents influence volatility. Here we describe the synthesis, structures, and thermal properties of a series of volatile lanthanide complexes (Ln = Nd, Er, and Yb) containing N_4O_3 ligands decorated with different alkyl and fluoroalkyl substituents (CF_3, $CF_2CF_2CF_3$, Me, and ^tBu). These ligands completely enveloped the tested lanthanides to form monomeric complexes with 7-coordinate distorted capped octahedral coordination geometries, as determined using single-crystal X-ray diffraction. Thermogravimetric analysis and bulk sublimation studies show how metal encapsulation affords complexes with the same volatility regardless of metal size, even with lanthanide ions with significantly different radii such as Nd^{3+} and Yb^{3+}. Most notably, the results show that increasing ligand fluorination, a strategy often used to increase the volatility of metal complexes, is not always beneficial and can significantly attenuate the volatility of lanthanide complexes depending on location with respect to other substituents in the ligand framework. A pair-wise model based on density functional theory shows that the net intermolecular interactions in the unit cell can still be stronger when fluorination is present. In other words, even if individual interactions between neighboring molecules are weaker, the total number of interactions in the solid arising from the nature of crystal packing is equally important to consider.

[a]*Department of Chemistry, The University of Iowa, E331 Chemistry Building, Iowa City, Iowa 52242, USA. E-mail: scott-daly@uiowa.edu*
[b]*Department of Chemistry, The University of South Dakota, 414 E Clark St, Vermillion, SD, 57069, USA*

†Electronic supplementary information (ESI) available: Crystallographic details and molecular structures of **Yb-2**, **Yb-4**, **Er-1**, and **Nd-3**. NMR and IR spectra, TGA plots. Interacting pairs from DFT calculations. CCDC 2313982–2313988. For ESI and crystallographic data in CIF or other electronic format see DOI: https://doi.org/10.1039/d3dt04198k
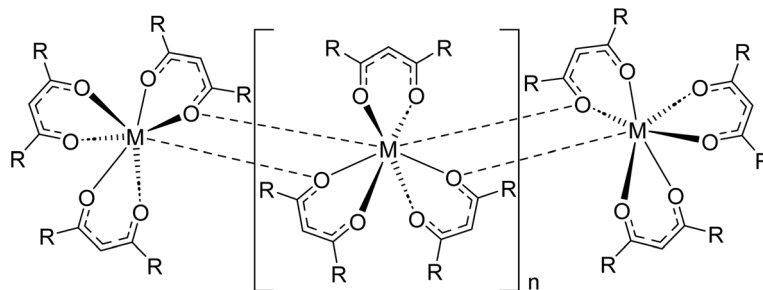
Introduction

Understanding chemical factors that give rise to changes in the volatility of lanthanide complexes is key to their development for applications such as chemical vapor deposition and separations *via* gas chromatography and thermochromatographic methods.[1–4] The ability to sublime or evaporate lanthanide complexes is often dictated first and foremost by coordinative saturation at the metal.[5] As compared to transition metals, trivalent lanthanides have relatively large coordination spheres and ionic metal–ligand bonding due to

their core-like 4f orbitals. As a result, ligands that have insufficient size to charge ratios often bridge adjacent lanthanides to completely saturate all available metal coordination sites (Fig. 1). These intermolecular bridging modes subsequently attenuate volatility because the lanthanide complexes must then depolymerize to form volatile molecular units that can escape into the gas phase. Even in the absence of formal bridging lanthanide–ligand bonds, accessible voids in the metal coordination sphere can lead to significant intermolecular interactions that suppress volatility. This has led researchers to adopt strategies such as using ancillary, L-type Lewis base donors, in some cases appending them directly to the ligand scaffold,[6,7] to fill remaining sites in the lanthanide coordination sphere. Additional anionic ligands can also be added in some cases to afford volatile complex salts, as observed for [Na(tetraglyme)][Ln(hfac)₄] (Ln = Y, Gd; hfac = hexafluoroacetylacetonate).[8]

The primary influence of coordinative saturation on the volatility of lanthanide complexes is apparent when looking at complexes that vary only in the size and identity of the lanthanide ion. It has been shown that the sublimation temperatures

Fig. 1 Coordination polymer of sterically undersaturated homoleptic lanthanide complexes, as represented with β-diketonate ligands. Adapted from ref. 1 with permission from Elsevier.

of homoleptic lanthanide complexes containing identical β-diketonate,[5,9–12] amides,[13] cyclopentadienyl,[14] or aminodiboranate ligands[15,16] decrease as the lanthanide series is traversed from large, early lanthanide ions like La^{3+}, Ce^{3+}, and Nd^{3+} to smaller, late lanthanides like Er^{3+}, Yb^{3+}, and Lu^{3+}. This change occurs primarily because smaller lanthanides are easier to coordinatively saturate, which can make it difficult to evaluate how electronic changes at the metal (particularly with respect to changing Lewis acidity) may also influence volatility.[17] Similarly, ligand modifications that alter substituent size and steric profile can also affect electronic properties. This is especially true when decorating complexes with C–F bonds, a common strategy for enhancing the volatility of metal complexes.[18] For example, exchange of CH_3 groups in the β-diketonate ligand acetylacetonate (acac) for fluorinated CF_3 groups in trifluoroacetylacetonate (tfac) and hexafluoroacetylacetonate (hfac) is known to yield a stepwise increase in the volatility of transition metal and aluminum β-diketonate complexes.[9] In contrast, it is difficult to assess how such stepwise changes in fluorination influence volatility in the same series of lanthanide β-diketonate complexes because only $Ln(hfac)_3$ are appreciably volatile.[19] Homoleptic $Ln(acac)_3$ complexes do not sublime and $Ln(tfac)_3$ complexes typically do so with significant decomposition, which is attributed to significant polymerization in the solid state, as shown in Fig. 1.[19]

We postulated that one way to better distinguish between steric and electronic substituent contributions to volatility in lanthanide complexes would be to fully encapsulate the metal ion using a single ligand. This would attenuate the possibility of intermolecular interactions so that electronic contributions to volatility could be assessed as a function of metal and ligand variations. The challenge is identifying a single trianionic ligand that not only fully encapsulates the metal to form a charge neutral complex, but also yields some volatility for testing. In general, there are few volatile lanthanide complexes containing ligands with denticities higher than three.[20] One of the only known examples that meets these criteria is the heptadentate ligand precursor tris[(4-hydroxypentenylidene-2-imino)ethyl]amine (H₃(TRAC), Fig. 2).[21] When deprotonated, TRAC is a trianionic N₄O₃ ligand best described as three β-ketoimate units tethered together by a tertiary amine linker. Orvig and co-
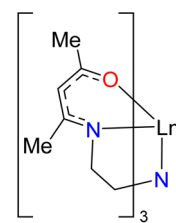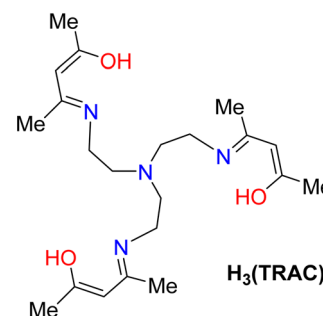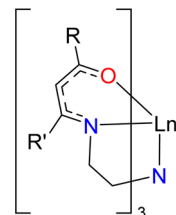

Fig. 2 Structure of lanthanide TRAC complexes prepared previously, and new fluorinated TRAC derivatives reported here.

workers showed that TRAC chelates trivalent lanthanide ions to form fully encapsulated metal complexes that can be sublimed, albeit at the relatively high temperature of 180 °C and 10^{-2} Torr.[21] Despite being first reported over 30 years ago, little has been done since then to investigate how ligand substitutions affect the volatility and thermal properties of these complexes.

Here we report the synthesis of a series of Nd, Er, and Yb complexes with differently-substituted TRAC ligands to investigate the effects of metal encapsulation, metal size, and ligand fluorination on complex volatility. These studies, which include thermogravimetric analysis (TGA) and single-crystal X-ray diffraction (XRD) studies, reveal unexpected trends that help distinguish between steric and electronic ligand contributions to the volatility of lanthanide TRAC complexes. Notably, the results show how fluorination, a common strategy for enhancing the volatility of complexes, can be detrimental to volatility depending on the location of fluorinated substitu-

ents within the structure. These results are supported by a set of density functional theory (DFT) calculations of pair-wise interactions that demonstrate how the nature and intensity of intermolecular interactions influence the ease with which these systems can be volatilized. The results show how fully encapsulating different sized lanthanides such as Nd and Yb with the same ligand yields complexes with no appreciable metal-size dependent differences in volatility. Finally, we describe competitive ligand binding studies with Nd and Yb to investigate how differences in metal–ligand reactivity may be used to achieve volatile separation of early and late lanthanides in mixtures.

Results and discussion

Synthesis and structures

Fluorinated H_3(TRAC) ligand precursors were synthesized as described for the parent H_3(TRAC) by treating tris(2-aminoethyl)amine (TREN) with an excess of the desired β-diketone (Scheme 1a).[22] Condensation reactions with hexafluoroacetylacetone, H(hfac), 1,1,1,5,5,6,6,7,7,7-decafluoro-4,6-heptanedione, H(dfhd), 1,1,1,2,2,3,3,3-heptafluoro-7,7-dimethyl-4,6-octanedione, H(fod), 1,1,1-trifluoroacetylacetone, H(tfac) (Chart 1) yielded the new protonated ligand precursors H_3(**1**) (R, R′ = CF_3), H_3(**2**) (R, R′ = $CF_2CF_2CF_3$, CF_3), H_3(**3**) (R, R′ = $CF_2CF_2CF_3$, ^tBu), and H_3(**4**) (R, R′ = CF_3, Me) respectively. Despite the different substituents, the reactions with unsymmetric β-diketones were quite selective, substituting almost exclusively at the carbon adjacent to the less electron-withdrawing substituent. Even the synthesis of H_3(**2**) with the similar fluoroalkyls R, R′ = $CF_2CF_2CF_3$, CF_3 was remarkably selective. However, we note that the synthesis of the mixed alkyl/fluoroalkyl ligands H_3(**3**) and H_3(**4**) were susceptible to formation of
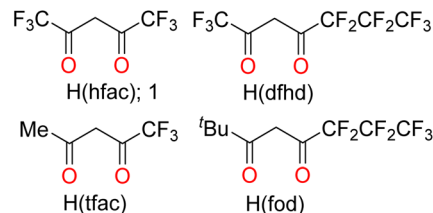

Chart 1 Substituted β-diketones used to prepare new fluorinated TRAC ligands.

amide-containing side products, especially when performing the reactions in the presence of 3 Å molecular sieves to scavenge water from the reactions. Several monoamide byproducts were isolated and structurally characterized (Fig. S5; ESI†).

The lanthanide complexes were prepared by mixing one equivalent of the corresponding protonated ligand precursor with one equivalent of Ln[N(SiMe$_3$)$_2$]$_3$ overnight (Scheme 1b). The protonolysis reactions proceeded smoothly in Et$_2$O at room temperature with all four ligands and Yb[N(SiMe$_3$)$_2$]$_3$, as well as for the reaction between Er[N(SiMe$_3$)$_2$]$_3$ and H_3(**1**). Similar reactions with Nd[N(SiMe$_3$)$_2$]$_3$ were not successful under the same conditions in Et$_2$O, but refluxing H_3(**3**) with Nd[N(SiMe$_3$)$_2$]$_2$ in toluene yielded **Nd-3**. The six new lanthanide complexes were isolated in good to excellent yields (82–94%) as single crystals by layering concentrated Et$_2$O solutions with pentane followed by cooling to −30 °C. Elemental analysis data collected on the crystals verified their composition and purity.

Single-crystal XRD data show that the lanthanide complexes adopt chiral seven-coordinate distorted capped octahedron coordination geometries. All of the crystallographically-characterized complexes crystallize with both Λ and Δ isomers in the unit cell, as reported previously for the structure of **Yb(TRAC)**
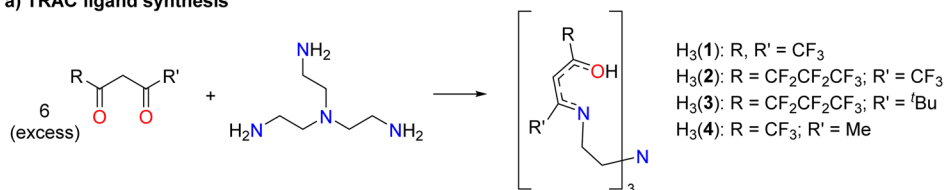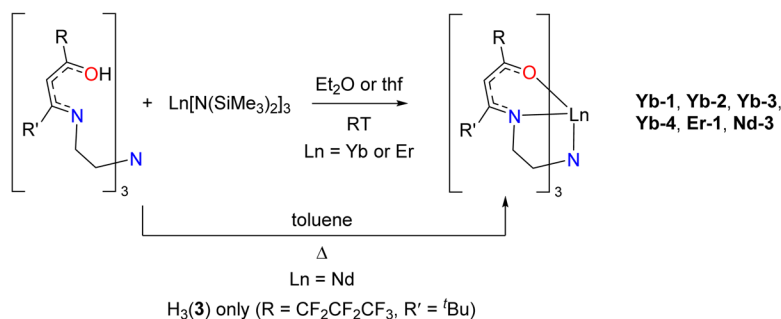
Scheme 1 (a) General synthesis and labeling scheme used for fluorinated TRAC ligands. (b) Protonolysis reactions with Ln[N(SiMe$_3$)$_2$]$_3$ (Ln = Nd, Er, Yb) and labeling scheme used for the prepared complexes.
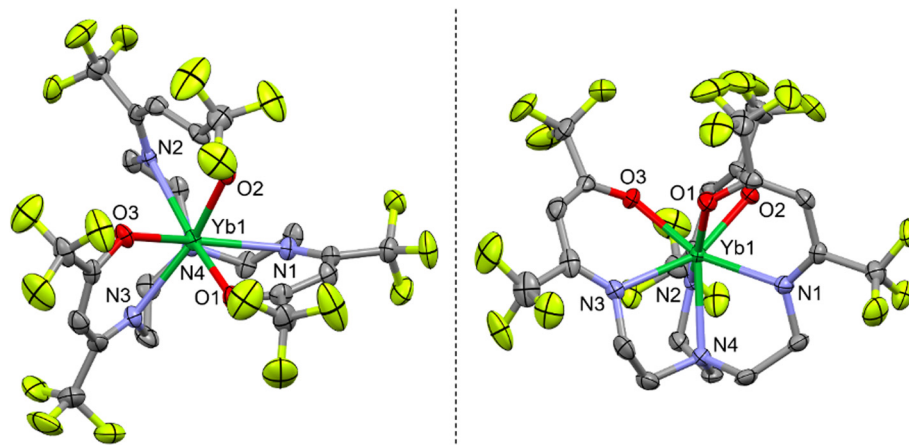
Fig. 3 Molecular structure of **Yb-1**. Left – Top view looking down the C_3 rotation axis defined Yb1–N4 bond. Right – Side-on view. Thermal ellipsoids are drawn at the 50% probability level. Hydrogen atoms were omitted from the figure. Select bond distances and angles: Yb1–O1 = 2.194(3) Å, Yb1–O2 = 2.177(3) Å, Yb1–O3 = 2.178(4) Å; Yb1–N1 = 2.430(6) Å, Yb–N2 = 2.421(4) Å, Yb–N3 = 2.427(5) Å, Yb–N4 = 2.474(5) Å. N1–Yb–O3 = 159.1 (1)°, N2–Yb–O1 = 160.5(1)°, N3–Yb–O2 = 157.9(1)°.

(Fig. 3).[21] The twist angle (φ), defined here as the rotation of the O and N triangular faces (Fig. 4), was determined to evaluate the deviation from capped octahedral towards capped trigonal prism as a function of metal and ligand substituents. This value was calculated using the C–N4–Ln–O and C–N4–Ln–N dihedral angles for each β-ketoiminate subunit (C is the carbon atom that tethers the associated β-ketoiminate subunit to the capping atom N4; see Fig. S48 in the ESI† for an example calculation and further details). The twist angles ranged from 51(1)°–56(2)° with the largest twist angles favoring complexes **Yb-1**, **Er-2**, and **Yb-2** with fully fluorinated CF_3 and $CF_2CF_2CF_3$ substituents (Table 1). The N4–Yb–N and N4–Yb–O angles with the capping amine N define the angles θ_2 and θ_5, as described by Hoffmann, Muetterties, and coworkers for capped octahedron coordination geometries (Fig. 4).[23] The lanthanide TRAC complexes exhibit θ_2 and θ_5 angles that are slightly more acute than the optimum 75° and 130° angles predicted for d^0 and d^4 transition metal complexes in the same coordination geometry (Table 1).[23]

The Yb–O bond distances are similar in all the complexes and unremarkable when compared to the parent **Yb(TRAC)** and homoleptic Yb β-ketoiminate complexes reported previously (Table 1).[21,24,25] The shortest Yb–O distances in the complexes reported here were found in **Yb-1** and range from
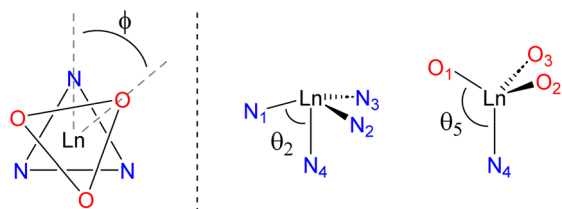
2.177(3)–2.194(3) Å, whereas the longest distances found in **Yb-4** range from 2.194(4)–2.198(4) Å. In contrast, the Yb–N distances are more sensitive to changes in fluorination and vary by as much as 0.07 Å. The Yb–N bond distances associated with the β-ketoiminate subunit (Yb–N1, Yb–N2, and Yb–N3) increase in the order of **Yb-2** < **Yb-1** < **Yb-4** ~ **Yb(TRAC)**, whereas the Yb–N4 distances associated with the amine decrease in the same order from 2.492(3) Å in **Yb-2** to 2.424(4) Å in **Yb-4**. The Ln–O and Ln–N bond distances for **Er-1** and **Nd-3** increase compared to the Yb complexes, as expected due to the increasing size of the lanthanide ions (Yb^{3+} = 0.868 Å; Er^{3+} = 0.89; Nd^{3+} = 0.983; coordination number = 6).[26] Like the Yb complexes, the bond distances in **Er-1** and **Nd-3** are comparable to other lanthanide β-ketoiminate complexes containing these metals.[7]

NMR studies

^{1}H and ^{19}F NMR spectra collected on the lanthanide complexes in C_6D_6 revealed paramagnetically shifted and broadened resonances consistent with their formulations and chelation of the ligands (Table 2). The ^{1}H NMR spectra, for example, revealed diastereotopic ethylene resonances diagnostic of ligand chelation, as has been shown for other complexes containing TREN-derived tripodal ligands.[27,28] The ^{19}F NMR spectra for **Yb-2**, **Yb-3**, and **Nd-3** also revealed diastereotopic CF_2 resonances from the $CF_2CF_2CF_3$ chain. No ^{1}H NMR resonances were observed for **Er-1**, presumably due to paramagnetic broadening, but ^{19}F resonances for the CF_3 substituents were observed for **Er-1** at δ −68.4 and −78.9 ppm in C_7D_8.

The most interesting finding from the NMR studies is that the degree of paramagnetic shifting in the Yb complexes depends significantly on the identity of the ligand substituents (Fig. 5). The ^{1}H resonances for **Yb-3** (R = $CF_2CF_2CF_3$ and R′ = ^tBu) are spread out over the widest spectral window, ranging from δ 60.7 to −12.7 ppm. In contrast, the resonances for **Yb-4** with R = Me and R′ = CF_3 fall within the narrow window of δ


Fig. 4 Left – The twist angle (φ) looking down the three-fold rotation axis (Λ isomer). Right – The θ_2 and θ_5 angles defined previously for 7-coordinate capped octahedral complexes.[23]

Table 1 Bond distances (Å) and angles (°) from single-crystal XRD studies

	Yb (TRAC)[21]	Yb-1	Yb-2	Yb-4	Er-1	Nd-3
M–O1	2.18(1)	2.194(3)	2.189(3)	2.198(4)	2.211(2)	2.304(2)
M–O2	2.161(9)	2.177(3)	2.181(2)	2.195(4)	2.222(3)	2.311(2)
M–O3	2.20(1)	2.178(4)	2.187(3)	2.197(4)	2.212(2)	2.301(2)
M–N1	2.46(1)	2.430(6)	2.408(3)	2.422(5)	2.443(3)	2.555(2)
M–N2	2.45(1)	2.421(4)	2.401(3)	2.457(4)	2.429(3)	2.577(2)
M–N3	2.44(1)	2.427(5)	2.408(3)	2.456(4)	2.459(2)	2.579(2)
M–N4	2.43(1)	2.474(5)	2.492(3)	2.424(4)	2.558(2)	2.641(1)
N–M–O$_{trans}$	162.8(4)	160.5(1)	165.5(1)	162.0(1)	167.62(9)	168.34(6)
	161.3(4)	159.1(1)	159.7(1)	161.3(1)	164.10(9)	166.90(6)
	159.1(4)	157.9(1)	157.9(1)	160.6(1)	159.65(9)	165.26(6)
N4–M–O1 (θ_5)	129.1(4)	127.5(1)	125.6(1)	127.4(1)	121.69(9)	122.29(5)
N4–M–O2 (θ_5)	126.7(4)	127.5(1)	130.3(1)	128.5(1)	129.22(9)	119.31(5)
N4–M–O3 (θ_5)	128.8(4)	129.2(1)	122.9(1)	128.9(1)	118.88(9)	120.77(5)
N4–M–N1 (θ_2)	69.8(4)	71.6(2)	71.5(1)	69.6(1)	70.74(9)	68.57(5)
N4–M–N2 (θ_2)	68.2(4)	71.5(2)	72.6(1)	68.9(1)	69.35(9)	69.39(5)
N4–M–N3 (θ_2)	69.0(4)	72.3(2)	71.8(1)	69.0(1)	70.18(9)	69.03(5)
Twist (φ)	51(1)	54(1)	56(2)	52(1)	55(5)	51(2)

Table 2 ^{1}H and ^{19}F NMR resonances (δ units in ppm) of lanthanide TRAC complexes in C$_6$D$_6$ at room temperature

Complex	^{1}H (methine)	^{1}H (ethylene)	^{19}F
[Yb(TRAC)]	−1.39	23.54, 17.51, 6.13, 5.82	—
Yb-1	−0.82	21.27, 10.75, 6.18	−71.5, −73.6
Yb-2	−4.18	34.10, 32.82, 11.33, 7.66	−74.8, −78.7, −111.3, −119.5, −122.3
Yb-3	−12.73	60.69, 59.17, 14.73, 10.88	−70.9, −114.1, −110.2, −120.0
Yb-4	1.92^a	6.49, 5.22, 4.73, 2.82	−76.4
Er-1	Not observed	Not observed	−68.4, −78.9^b
Nd-3	−18.11	12.75, 0.53, −3.27, −13.39	−86.7, −115.8, −131.0

^{a} Tentative assignment. ^{b} Collected in C$_7$D$_8$.
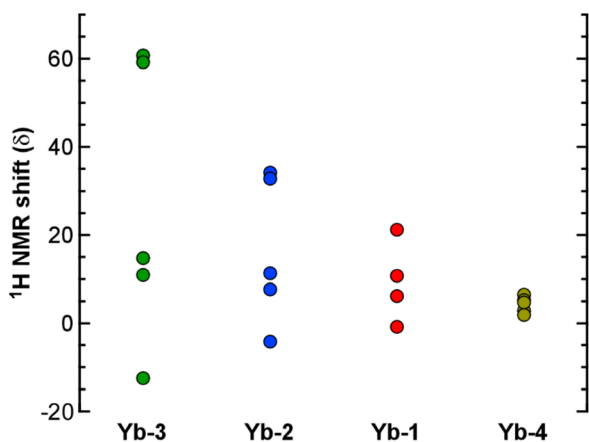
Fig. 5 Methine and ethylene ^{1}H NMR shifts for the Yb complexes.

6.49 to 1.92 ppm, and the spectral range decreases in the order **Yb-3** > **Yb-2** > **Yb-1** > **Yb-4**. Given their position with respect to Yb, the paramagnetic NMR shifts for the ^{1}H nuclei are likely governed by the "through-space" pseudocontact shift (as opposed to the "through-bond" contact shift).[29] Parker and coworkers recently showed how changing pyridyl substituents in 9-coordinate, tricapped trigonal prismatic Yb complexes yielded similarly dramatic changes in the ^{1}H pseudocontact shifts that were attributed to the influence of ligand dipolar polarizability and solvation on ligand field strength.[30] We suspect that a similar phenomenon is operative in the Yb complexes reported here, but further studies will be needed to evaluate this hypothesis. For example, quantifying these sorts of ligand field contributions has been achieved by preparing Eu complexes with the same ligands and measuring their emission spectra.[30]

Volatility studies

Thermogravimetric analysis (TGA) and bulk sublimation studies were carried out on all the fluorinated TRAC complexes to determine the influence of substituent modifications and metal identity on complex volatility (Fig. 6). The parent **Yb (TRAC)** was also prepared and used as a benchmark for comparison. The TGA studies were carried out at atmospheric pressure under a slow purge of N$_2$ gas whereas bulk sublimation studies were carried out under vacuum at 10^{-2} Torr. Volatility assessments using TGA were determined by taking the 1st derivative of the TGA curves to quantify the temperature of maximum % weight loss (Fig. S38–S44; ESI†).

The TGA and bulk sublimation studies of the Yb complexes follow the same trend, and show that volatility decreases in the order **Yb-1** ∼ **Yb-2** > **Yb(TRAC)** ∼ **Yb-3** > **Yb-4** (Table 4). **Yb-1**, **Yb-2**, and **Yb-3** volatilize cleanly with relatively little thermal decomposition, as indicated by >95% weight loss by TGA and during sublimation studies (Fig. 6). **Yb-1** and **Yb-2** with fully fluorinated substituents are the most volatile, with TGA weight loss maxima of 222 and 225 °C, respectively. Likewise, both complexes are similarly volatile when heated under vacuum, subliming at 120 °C at 10^{-2} Torr. These results indicate that increasing the length of the fluoroalkyl chains from CF$_3$ in **Yb-1** to CF$_2$CF$_2$CF$_3$ in **Yb-2** has a negligible impact on volatility despite that higher molecular weight typically portends decreased volatility *via* increased number of intermolecular forces. For comparison, weight loss maxima and sublimation temperatures for **Yb(TRAC)** with R, R′ = Me were *ca.* 40 °C higher than **Yb-1** and **Yb-2** at 261 and 160 °C, respectively. Notably, the 160 °C sublimation temperature of **Yb(TRAC)** at 10^{-2} Torr in our hands occurs even lower than the 180 °C at 10^{-2} Torr reported previously.[21] **Yb-3** with R = CF$_2$CF$_2$CF$_3$ and R′ = ^{t}Bu shows similar volatility as the parent **Yb(TRAC)** complex with a sublimation max of 269 °C by TGA and a bulk sublimation temperature of 160 °C under vacuum.

The most unexpected result was observed with **Yb-4** with R = CF$_3$ and R′ = Me. This complex is the least volatile in the series despite increased fluorination with respect to **Yb(TRAC)** and decreased molecular weight compared to **Yb-3** (which also
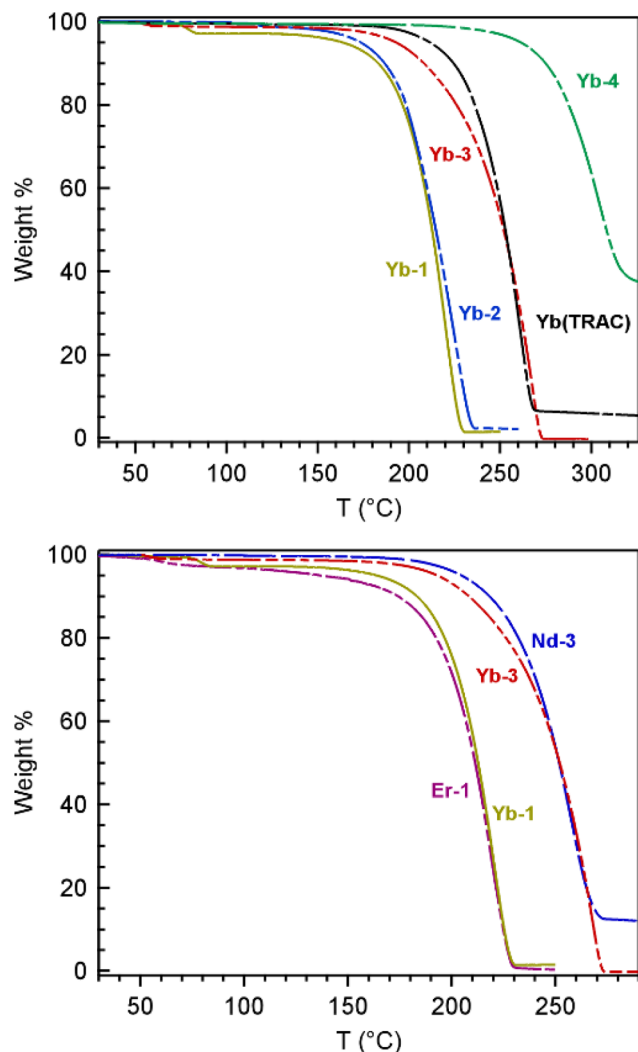
Fig. 6 Top —TGA comparison of the Yb complexes: **Yb-1** (gold), **Yb-2** (blue), **Yb-3** (red), **Yb-4** (green), and [**Yb(TRAC)**] (black). Bottom – TGA comparison of lanthanide complexes with different metals: **Yb-1** (gold) *vs.* **Er-1** (magenta) and **Yb-3** (red) *vs.* **Nd-3** (blue).

Table 3 Comparison of sublimation max temperatures at atmospheric pressure, as measured by weight loss using thermogravimetric analysis, and sublimation temperatures under vacuum

Complex	Weight loss max (TGA)	Sublimation T (10^{-2} Torr)
Yb-1	222 °C	120 °C
Er-1	221 °C	120 °C
Yb-2	225 °C	120 °C
Yb(TRAC) [a]	261 °C	160 °C
Nd-3	263 °C	160 °C
Yb-3	269 °C	160 °C
Yb-4	306 °C	190 °C

[a] Prior studies report bulk sublimation at 180 °C at 10^{-2} Torr. In our hands, this complex sublimes at temperatures as low as 160 °C at 10^{-2} Torr.

cant difference in ligand dipolar polarizability, which lends support for this hypothesis.

Next, we compare the TGA and sublimation data for **Yb-1**/**Er-1** and **Nd-3**/**Yb-3** complexes containing the same ligand, but different metals. We see no significant differences in volatility when the metal is varied, which is most notable for **Nd-3** and **Yb-3** given the relatively large differences in metal size and Lewis acidity (Table 3). This finding corroborates previous reports showing that Ln(TRAC) complexes with Ln = Sm, Er, and Yb sublime at identical temperatures.[21] Collectively, these results suggest that encapsulation of the metal imparts similar volatility regardless of metal size, which is markedly different compared to most lanthanide complexes, as described in the introduction.

Computational analysis of Yb complexes

Density functional theory (DFT) calculations were performed (PBE0-D3/def2-TZVP) to build a lattice model to better understand the observed differences in the volatility of the Yb complexes. Initial assessment of the crystallographic parameters suggested that the differences cannot be attributed solely to differences in crystal packing. For example, the experimental data shows that the most volatile (**Yb-1**) and the least volatile (**Yb-4**) have similar atomic packing factor (APF) values, 9.7 and 9.5%, respectively. However, the APF of **Yb(TRAC)**, which is the system with intermediate volatility, is 11.0%. Therefore, to better understand the volatilization tendency between the Yb complexes, we needed to evaluate both the strength and quantity of intermolecular interactions. We carefully analyzed all pair-wise interactions of nearest neighbor complexes in the crystal structures of **Yb-1**, **Yb(TRAC)**, and **Yb-4**. Non-covalent interaction energies were measured in a 2 × 2 × 2 supercell for contacts that gave intermolecular Yb···Yb distances less than 11 Å, *i.e.*, distances with significant intermolecular interaction energies. This analysis revealed different numbers of intermolecular pairs, or dimers, in the supercell with Yb···Yb distances less than 11 Å: six in **Yb-1**, eleven in **Yb(TRAC)**, and four in **Yb-4** (Table 4 and Fig. S45–S47†).

As noted above, swapping CH_3 groups for CF_3 gives rise to different solid-state structures, including the arrangement and

contains alkyl and fluoroalkyl substituents in the same positions). TGA of **Yb-4** shows a maximum % weight loss at 306 °C, but this is at least partly attributed to decomposition because the trace levels off after ~60% weight loss. **Yb-4** sublimes more cleanly under vacuum at 190 °C, which is 30 °C higher than **Yb-3** and **Yb(TRAC)** under the same conditions. We tentatively attribute the lower volatility of **Yb-4** to the unsymmetric alkyl and fluoroalkyl substituents that enhances intermolecular attractive forces in the solid state *via* an increased dipole across the complex. It seems likely that a similar dipole increase is present in **Yb-3**, but the larger ^{t}Bu and $CF_2CF_2CF_3$ substituents appear to diffuse the strength of this dipole and/or shield the positively charged metal from significant attractive intermolecular interactions with polarized ligand fragments. The spectral width of the paramagnetic ^{1}H NMR shifts described in the previous section, which are largest for **Yb-3** and smallest for **Yb-4**, indeed suggest a signifi-

Table 4 Non-covalent interactions (E_{inter}) between the nearest monomers forming **Yb-1**, **Yb(TRAC)**, and **Yb-4**. The Yb⋯Yb distance (r) of each dimer is in Å, and the total number of neighboring dimers (n) included in a 2 × 2 × 2 supercell. The average interaction energies per unit cell are between parentheses. Energies are in kcal mol⁻¹

Yb-1				Yb(TRAC)				Yb-4			
r(Yb⋯Yb)	E_{inter}	n	Total E_{inter}	r(Yb⋯Yb)	E_{inter}	n	Total E_{inter}	r(Yb⋯Yb)	E_{inter}	n	Total E_{inter}
8.73	−16.3	26	−423.6	7.61	−13.7	32	−439.2	7.91	−17.4	80	−1393.7
8.79	−12.0	60	−718.6	7.64	−12.7	16	−203.2	9.22	−24.7	38	−937.4
10.02	−2.6	44	−114.7	8.13	−12.0	24	−288.3	10.02	−7.6	80	−610.5
10.30	−5.6	48	−268.0	8.78	−8.9	24	−214.4	10.81	−0.9	37	−31.9
10.85	−5.0	29	−144.3	8.86	−7.3	12	−87.5				
10.98	−2.0	24	−47.6	8.93	−7.6	4	−30.5				
				9.19	−2.2	10	−21.8				
				10.31	−2.4	12	−28.6				
				10.36	−3.1	12	−37.5				
				10.47	−0.7	24	−17.8				
				10.52	−1.0	24	−23.1				
			−1716.7 (**−6.1**)				−1391.9 (**−7.2**)				−2973.6 (**−12.7**)

packing, and this corresponds to changes in the types of intermolecular interactions in the crystal. In both **Yb-1** and **Yb(TRAC)**, the dominant intermolecular interactions take place between the CF_3 or CH_3 groups of one complex and the O and N atoms in a neighboring complex. Weaker F⋯F and F⋯H contacts are present in **Yb-1**, and between CH_3 and the Schiff arms in the case of **Yb(TRAC)** (Fig. S45 and S46†). The case of **Yb-4** is unique in that the interactions primarily occur between alkyl and CF_3 groups except for a single CH_3⋯carbonyl interaction (Fig. S47†). This suggests that replacing only half of the CH_3 groups in **Yb(TRAC)** for CF_3 results in preferred interactions between these groups in neighboring complexes.
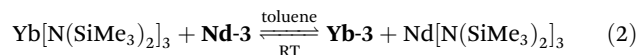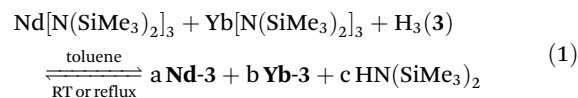
In addition to having differing numbers and type of contacts, the calculations revealed significant differences in their strengths. The non-covalent interaction (NCI) index was computed to identify and quantify the interactions between neighboring moieties in each crystal (Table 4). Noticeably, the strength of interactions between neighboring fragments of **Yb-1** and **Yb(TRAC)** are similar, but the number of instances for the latter is significantly larger. Taking both number and strength yields average interaction energies of −6.1 kcal mol⁻¹ for **Yb-1** and −7.2 kcal mol⁻¹ for **Yb(TRAC)**, consistent with the higher volatility of **Yb-1**. On the other hand, **Yb-4** has the strongest and largest number of intermolecular interactions, yielding an average interaction energy of −12.7 kcal mol⁻¹, consistent with it having the lowest volatility in the series. Overall, this simple lattice model supports that the net intermolecular interactions are strongest in **Yb-4** and follow the order **Yb-4** > **Yb(TRAC)** > **Yb-1** in agreement the observed differences in volatility.

Competitive ligand binding and reactivity studies

The similarities in volatility for **Nd-3** and **Yb-3** provided an opportunity to investigate if differences in metal–ligand reactivity and ligand binding affinity could be used to achieve volatile separation of early and late lanthanides using **3**. As discussed in the introduction, many lanthanide complexes show metal size-dependent differences in volatility that could be used to achieve a separation using methods such as GC or thermochromatography. When there are no significant metal-size dependent differences in complex volatility, as described here, another potential way to achieve volatile separation of lanthanides is to exploit differences in metal–ligand reactivity, as is typically done with selective solvent-based extractants.

To investigate this possibility, we examined reactions with one equivalent of $Nd[N(SiMe_3)_2]_3$, $Yb[N(SiMe_3)_2]_3$, and H_3(**3**) under different time and temperature conditions (eqn (1)). The resulting mixtures were then evaporated to dryness, the volatile products were sublimed at ~160 °C at 10⁻² Torr until no additional material was observed to deposit on the cold finger from the residue (~2 hours), and the sublimate was analyzed by ¹⁹F NMR spectroscopy to quantify the distributions of products containing **3**. We note that the $Ln[N(SiMe_3)_2]_3$ starting materials used in these studies are also volatile and will certainly sublime to some extent under the tested conditions. This is obviously not desirable from the perspective of lanthanide separations, but the experiment design meets the intended purpose of understanding binding and reactivity preferences of **3** with different lanthanides.

$$Nd[N(SiMe_3)_2]_3 + Yb[N(SiMe_3)_2]_3 + H_3(\mathbf{3})$$
$$\xrightleftharpoons[\text{RT or reflux}]{\text{toluene}} a\,\mathbf{Nd\text{-}3} + b\,\mathbf{Yb\text{-}3} + c\,HN(SiMe_3)_2 \quad (1)$$

$$Yb[N(SiMe_3)_2]_3 + \mathbf{Nd\text{-}3} \xrightleftharpoons[\text{RT}]{\text{toluene}} \mathbf{Yb\text{-}3} + Nd[N(SiMe_3)_2]_3 \quad (2)$$

The competition reactions of one equivalent of $Nd[N(SiMe_3)_2]_3$, $Yb[N(SiMe_3)_2]_3$, and H_3(**3**), as represented by eqn (1), were performed in toluene under three different conditions: stirring at RT for 1 h, stirring at RT for 24 h, and refluxing for 24 h (Table 5 and Fig. S27–S29; ESI†). The reaction performed at 1 h at RT revealed preferential formation of **Yb-3** with the smaller Yb^{3+} ion: the relative distribution of **Yb-3** to **Nd-3** was 5 : 1 and 34% of the $Yb[N(SiMe_3)_2]_3$ was converted to **Yb-3** compared to 7% for **Nd-3**. After 24 h, the distribution remains roughly the same with the conversions of **Yb-3** and **Nd-3** increasing to 47% and 10%, respectively. By contrast,

Table 5 Sublimed product distributions from competition reactions represented by eqn (1) at different time intervals and temperatures. Relative distributions were quantified using the ^{19}F resonances of the terminal CF_3 substituents

Reaction conditions	Yb-3	Nd-3	Unreacted H$_3$(3)
1 h/RT	34%	7%	59%
24 h/RT	47%	10%	43%
24 h/reflux	38%	48%	14%

refluxing the mixture for 24 h results in a marked increase of **Nd-3** (48%) relative to **Yb-3** (38%), and almost complete consumption of H$_3$(**3**).

It was not clear if the preferential conversion to **Nd-3** at higher temperatures was a consequence of kinetic or thermodynamic factors, so additional experiments were performed to better evaluate the thermodynamic binding preference of **3** with Nd and Yb relative to their corresponding Ln[N(SiMe$_3$)$_2$]$_3$ complexes. Competition experiments were performed by stirring **Nd-3** with Yb[N(SiMe$_3$)$_2$]$_3$ and **Yb-3** with Nd[N(SiMe$_3$)$_2$]$_3$ in toluene for 24 h at RT (eqn (2)). No formation of **Nd-3** was observed in the mixture containing **Yb-3** and Nd[N(SiMe$_3$)$_2$]$_3$ but a small amount **Yb-3** (~6%) corresponding to ligand exchange was observed in the mixture containing **Nd-3** and Yb[N(SiMe$_3$)$_2$]$_3$ (Fig. S30 and S31; ESI†). This result suggests that there is a greater thermodynamic preference for **Yb-3** and Nd[N(SiMe$_3$)$_2$]$_3$.

Conclusion

In summary, we have described the synthesis, structures, and thermal properties of heptadentate lanthanide complexes containing fluorinated N$_4$O$_3$ ligands derived from TRAC. These encapsulating ligands allowed the influence that fluorinated substituents and metal identity have on the volatility of lanthanide complexes to be quantified without competing intermolecular bonding and steric saturation effects. As reported previously for Ln(TRAC) complexes with Ln = Sm, Er, and Yb, no significant metal-size dependent differences in volatility were observed, which was most notable with **Nd-3** and **Yb-3** given the relatively large difference in metal ion size. These results suggest that lanthanide identity has little influence on volatility in the absence of solid-state oligomerization.

Studies of the differently-substituted Yb complexes reported here show how complexes with fully fluorinated substituents afford significant volatility enhancements when compared to non-fluorinated **Yb(TRAC)**, consistent with the expected result. Substituting the Me substituents in **Yb(TRAC)** for CF$_3$ and CF$_2$CF$_2$CF$_3$ in **Yb-1** and **Yb-2** lowered the sublimation temperature of both complexes by 40 °C. However, intermediate fluorination of the TRAC framework caused the opposite effect and was remarkably detrimental to the volatility of **Yb-4**, increasing its sublimation temperature by 30 °C with respect to **Yb (TRAC)**. A lattice model based on DFT calculations suggests that the reduced propensity to volatilization is due to stronger

interactions between CF$_3$ and CH$_3$ groups of neighboring fragments. This observation is in striking contrast with TGA studies reported previously for homoleptic transition metal and aluminum β-diketonates that show stepwise increases in volatility with increasing fluorination in the order of M(acac)$_3$ < M(tfac)$_3$ < M(hfac)$_3$ (M = Al, Cr. Fe, and Rh) with the same substituent combinations as **Yb(TRAC)** (R, R′ = Me), **Yb-4** (R = CF$_3$, R′ = Me), and **Yb-1** (R, R′ = CF$_3$).[9] Collectively, these studies show how ligand fluorination does not necessarily guarantee an increase in the volatility of lanthanide complexes.

Experimental

General considerations

All reactions were carried out under an atmosphere of N$_2$ or Ar using glovebox or standard Schlenk techniques unless stated otherwise. All glassware was heated at 150 °C for at least two hours and allowed to cool under vacuum before use. Except for those used for chromatography, solvents were dried and deoxygenated using a Pure Process Technologies Solvent Purification System and stored over 3 Å molecular sieves. Deuterated solvents were deoxygenated on the Schlenk line with five freeze–pump–thaw cycles and stored over 3 Å molecular sieves for at least three days before use. H$_3$(TRAC) and **Yb (TRAC)** were prepared from commercially available starting materials using the method described by Orvig and coworkers.[21,22] Nd[N(SiMe$_3$)$_2$]$_3$, Er[N(SiMe$_3$)$_2$]$_3$, and Yb[N (SiMe$_3$)$_2$]$_3$ were prepared by the method described by Bradley and coworkers.[31] Reagents and chromatography solvents were purchased from commercial vendors and used as received.

^{1}H NMR data were collected on a Bruker AVANCE-300 or DPX-300 operating at 300 MHz, a Bruker AVANCE-400 operating at 400 MHz, or a Bruker AVANCE-500 operating at 500 MHz. The ^{19}F NMR data were collected on a Bruker AVANCE-300 or DPX-300 operating at 282 MHz, a Bruker AVANCE-400 operating at 377 MHz, or a Bruker AVANCE-500 operating at 470 MHz. Chemical shifts are reported in δ units relative to residual NMR solvent peaks (^{1}H) or 10% fluorobenzene in C$_6$D$_6$ (^{19}F; δ −62.9 ppm). Microanalytical data (CHN) were collected using an EAI CE-440 elemental analyzer at the University of Iowa's Shared Instrumentation Facility. IR spectra were acquired with a Thermo Scientific Nicolet iS5 using an ATR accessory with a diamond crystal.

Thermogravimetric analysis data were collected on a TA Instruments Q500 TGA. Samples were transferred from the glovebox in a sealed container and quickly loaded in air. N$_2$ was used as the purge gas. The balance purge flow was set to 10 mL min^{-1}, and the sample purge was set to 90 mL min^{-1}. The ramp rate for all samples was set to 2 °C min^{-1} with a start point at room temperature and an equilibration point set between 260 and 350 °C. Melting points were determined in capillaries sealed under N$_2$ using a REACH MP device.

H$_3$(2). Tris(2-aminoethyl)amine (0.16 mL, 1.1 mmol) and 1,1,1,5,5,6,6,7,7,7-decafluoro-4,6-heptanedione (1.37 mL,

6.49 mmol) were added to toluene (50 mL). The solution became yellow and then turned light pink. The mixture was refluxed with stirring overnight, during which time the mixture turned dark brown. The mixture was allowed to cool to RT, filtered, and evaporated to dryness under vacuum. The residue was purified in air by column chromatography on silica gel (60–200 mesh; 60 Å pore size) using 50% ethyl acetate and 50% hexane as an eluent. The collected fraction was evaporated to dryness, and the oily residue was dissolved in the minimum amount of pentane. Cooling yielded a white solid. Yield: 0.29 g (27%). ^{1}H NMR (300 MHz, CDCl$_3$): δ 10.7 ppm (br s, 3H, OH), 5.86 ppm (s, 3H, CH), 3.63 ppm (q, 6H, CH$_2$), 2.87 ppm (t, 6H, CH$_2$). ^{19}F NMR (282 MHz, CDCl$_3$): δ −65.7 ppm (s, 3F, CF$_3$), −78.9 ppm (t, 3F, CF$_3$), −119.4 ppm (d, 2F, CF$_2$), −125.1 ppm (s, 2F, CF$_2$).

H$_3$(3). Tris(2-aminoethyl)amine (0.169 mL, 1.13 mmol) and 1,1,1,2,2,3,3-heptafluoro-7,7-dimethyl-4,6-octanedione (1.57 mL, 6.75 mmol) were added to toluene (10 mL) and the mixture was refluxed with stirring overnight. The mixture was allowed to cool to RT and then evaporated to dryness under vacuum. The mixture was extracted in air with a minimum amount of Et$_2$O, layered with pentane, and cooled to −30 °C to yield white blocks. Yield: 0.694 g (84%). ^{1}H NMR (500 MHz, CDCl$_3$): δ 11.9 ppm (br s, 3H, OH), 5.46 ppm (s, 3H, CH), 3.74 ppm (s, 6H, CH$_2$), 2.83 ppm (s, 6H, CH$_2$), 1.28 ppm (s, 27H, ^{t}Bu). ^{19}F NMR (377 MHz, CDCl$_3$): δ −86.7 ppm (s, 3F, CF$_2$), −115.9 ppm (br d, 2F, CF$_2$), −131.0 ppm (s, 2F, CF$_2$).

H$_3$(1). Prepared as described for H$_3$(3) using tris(2-amino-ethyl)amine (5.67 mL, 41.0 mmol) and hexafluoroacetylacetone (1.02 mL, 6.84 mmol). Yield: 1.19 g (25%). ^{1}H NMR (500 MHz, CDCl$_3$): δ 10.6 ppm (br s, 3H, OH), 5.80 ppm (s, 3H, CH), 3.62 ppm (t, 6H, CH$_2$), 2.88 ppm (t, 6H, CH$_2$). ^{19}F NMR (377 MHz, CDCl$_3$): δ −67.4 ppm, −77.5 ppm.

H$_3$(4). Tris(2-aminoethyl)amine (0.204 mL, 1.37 mmol) and 1,1,1-trifluoroacetylacetone (1.0 mL, 8.2 mmol) were added to toluene (30 mL). The mixture was refluxed with stirring overnight and then 3 Å molecular sieves were added. Note: we found it important to follow these steps exactly to minimize the formation of difficult to remove side products. The mixture was again refluxed for 2 h and then allowed to cool to RT. The mixture was filtered in air, evaporated to dryness under vacuum, washed with 50 mL of pentane, and again evaporated to dryness to yield a reddish-yellow solid. The solid was extracted with Et$_2$O (60 mL), evaporated again to dryness, and the solid was washed again with pentane (10 mL). The solid was dissolved in Et$_2$O (15 mL) and layered with pentane. Layering yielded a yellow solid that was no longer Et$_2$O soluble. The solid was washed with 80 mL of Et$_2$O and evaporated to dryness. Yield: 0.22 g (29%). ^{1}H NMR (300 MHz, CDCl$_3$): δ 11.19 ppm (br s, 3H, OH), 5.28 ppm (s, 3H, CH), 3.51 ppm (q, 6H, CH$_2$), 2.89 ppm (t, 6H, CH$_2$), 2.06 ppm (s, 9H, CH$_3$). ^{19}F NMR (282 MHz, CDCl$_3$): −77.2 ppm.

Yb-1. Yb[N(SiMe$_3$)$_2$]$_3$ (0.100 g, 0.153 mmol) and H$_3$(1) (0.109 g, 0.153 mmol) were dissolved in Et$_2$O and stirred for 2 h. The solution was evaporated to dryness under vacuum to yield a yellow-orange powder. The powder was redissolved in

the minimum amount of Et$_2$O, layered with pentane, and the mixture was stored at −30 °C to yield pale-yellow crystals. Yield: 0.123 g (91%). Mp: 245 °C. Subl. Temp. 120 °C (10^{-2} Torr). Anal. Calcd for C$_{12}$H$_{15}$F$_{18}$N$_4$O$_3$Yb: C, 28.46; H, 1.71; N, 6.32. Found: C, 28.45; H, 1.95; N, 6.15. ^{1}H NMR (500 MHz, C$_6$D$_6$): δ 21.2 ppm (br s, 6 H, CH$_2$), 10.7 ppm (br s, 3 H, CH$_2$), 6.18 ppm (br s, 3 H, CH$_2$), −0.82 ppm (s, 3 H, CH). ^{19}F NMR (377 MHz, C$_6$D$_6$): δ −71.5 ppm (s), −73.6 ppm (s). IR (cm^{-1}) 3181 (w), 3010 (w), 2950 (w), 2892 (w), 2168 (w), 1625 (s), 1608 (w), 1545 (s), 1517 (m), 1478 (s), 1471 (s), 1316 (s), 1267 (s), 1263 (s), 1192 (s), 1173 (s), 1149 (s), 1125 (s), 1110 (s), 1060 (s), 1031 (s), 966 (w), 947 (m), 917 (m), 867 (m), 848 (m), 792 (s), 737 (s), 663 (s).

Er-1. Prepared as described for **Yb-1** with Er[N(SiMe$_3$)$_2$]$_3$ (0.100 g, 0.154 mmol) and H$_3$(1) (0.110 g, 0.154 mmol). Layering yielded purple crystals. Yield: 0.115 g (85%). Mp: 245 °C. Anal. Calcd for C$_{12}$H$_{15}$ErF$_{18}$N$_4$O$_3$: C, 28.64; H, 1.72; N, 6.36. Found: C, 27.99; H, 1.97; N, 6.63. ^{19}F NMR (470 MHz, C$_7$D$_8$): δ −68.4 ppm (s), −78.9 ppm (s). IR (cm^{-1}) 2962 (w), 2875 (w), 2189 (w), 1684 (w), 1626 (m), 1599 (w), 1545 (m), 1535 (w), 1474 (m), 1383 (w), 1316 (m), 1269 (s), 1253 (s), 1175 (s), 1123 (s), 1092 (s), 1059 (s), 1027 (s), 943 (m), 914 (m), 866 (m), 847 (s), 793 (s), 736 (s), 663 (s).

Yb-2. Prepared as described for **Yb-1** with Yb[N(SiMe$_3$)$_2$]$_3$ (0.0875 g, 0.134 mmol) and H$_3$(2) (0.136 g, 0.134 mmol). Yield: 0.129 g (90%). Mp: 245 °C. Subl. Temp. 120 °C at 10^{-2} Torr. Anal. Calcd for C$_{28}$H$_{24}$F$_{23}$N$_4$O$_3$Yb: C, 27.33; H, 1.27; N, 4.72. Found: C, 27.74; H, 1.34; N, 4.79. ^{1}H NMR (500 MHz, C$_6$D$_6$): δ 34.1 ppm (br s, 3 H, CH$_2$), 32.8 ppm (br s, 3 H, CH$_2$), 11.3 ppm (br s, 3 H, CH$_2$), 7.66 ppm (br s, 3 H, CH$_2$), −4.18 ppm (s, 3 H, CH). ^{19}F NMR (377 MHz, C$_6$D$_6$): δ −74.8 ppm (s), −78.7 ppm (s), −111.3 ppm (d), −119.5 ppm (d), −122.3 ppm (s). IR (cm^{-1}) 3175 (w), 3010 (w), 2882 (w), 2168 (w), 2046 (w), 1617 (s), 1534 (s), 1479 (s), 1349 (m), 1309 (w), 1198 (s), 1142 (s), 1114 (s), 1059 (s), 1031 (s), 966 (s), 959 (m), 924 (m), 902 (m), 844 (m), 839 (w), 795 (s), 749 (s), 677 (w).

Yb-3. Prepared as described for **Yb-1** with Yb[N(SiMe$_3$)$_2$]$_3$ (0.100 g, 0.153 mmol) and H$_3$(3) (0.150 g, 0.153 mmol). Yield: 0.141 g (82%). Mp: 210 °C. Subl. Temp. 160 °C at 10^{-2} Torr. Anal. Calcd for C$_{36}$H$_{42}$F$_{21}$N$_4$O$_3$Yb: C, 37.57; H, 3.68; N, 4.87. Found: C, 38.2; H, 3.96; N, 5.14. ^{1}H NMR (500 MHz, C$_6$D$_6$): δ 60.7 ppm (br s, 3 H, CH$_2$), 59.2 ppm (br s, 3 H, CH$_2$), 14.73 ppm (br s, 3 H. CH$_2$), 10.9 ppm (br s, 3 H, CH$_2$), −9.69 ppm (s, 27 H, C(CH$_3$)$_3$), −12.7 ppm (s, 3 H, CH). ^{19}F NMR (470 MHz, C$_6$D$_6$): δ −70.9 ppm (s), −110.2 ppm (d), −114.1 ppm (q), −120.0 ppm (d). IR (cm^{-1}) 3173 (w), 2978 (w), 2933 (w), 2876 (w), 1161 (s), 1512 (s), 1496 (m), 1403 (w), 1371 (w), 1346 (m), 1225 (s), 1191 (s), 1164 (s), 1138 (s), 1135 (s), 1065 (s), 1037 (m), 965 (s), 917 (s), 835 (s), 784 (m), 750 (s), 680 (w), 644 (w).

Nd-3. Nd[N(SiMe$_3$)$_2$]$_3$ (0.100 g, 0.160 mmol) and H$_3$(3) (0.157 g, 0.160 mmol) were dissolved in toluene and refluxed for 2 h. The solution was evaporated to dryness under vacuum to yield a light blue powder. The powder was redissolved in the minimum amount of Et$_2$O, layered with pentane, and the mixture was stored at −30 °C to yield blue crystals. Yield:

0.168 g (94%). Mp: 210 °C. Subl. Temp. 160 °C at 10^{-2} Torr. Anal. Calcd for $C_{36}H_{42}F_{21}N_4NdO_3$: C, 38.54; H, 3.77; N, 4.99. Found: C, 37.22; H, 3.82; N, 5.06. ^{1}H NMR (500 MHz, C_6D_6): δ 12.8 ppm (s, 3 H, CH), 4.81 ppm (s, 27 H, $C(CH_3)_3$), 0.53 ppm (br s, 3 H, CH_2), −3.27 ppm (br s, 3 H, CH_2), −13.4 ppm (br s, 3 H, CH_2), −18.1 ppm (br s, 3 H, CH_2). ^{19}F NMR (470 MHz, C_6D_6): δ −86.7 ppm (s), −115.8 ppm (b), −131.0 ppm (s). IR (cm^{-1}) 3410 (b), 2976 (w), 2911 (w), 1613 (s), 1522 (s), 1454 (m), 1403 (w), 1374 (w), 1344 (m), 1221 (s), 1201 (s), 1174 (s), 1140 (s), 1106 (s), 1086 (m), 1032 (m), 965 (m), 904 (s), 829 (m), 786 (m), 747 (s), 704 (w), 677 (w), 637 (w).

Yb-4. $Yb[N(SiMe_3)_2]_3$ (0.240 g, 0.160 mmol) and H_3(**4**) (0.200 g, 0.160 mmol) were stirred in THF overnight. The solution was evaporated to dryness under vacuum to yield a pale-yellow powder. The powder was then redissolved in the minimum amount of Et_2O, layered with pentane, and the mixture was stored at −30 °C. Yield: 0.227 g (87%). Mp: 250 °C. Subl. Temp. 190 °C at 10^{-2} Torr. Anal. Calcd for $C_{36}H_{42}F_{21}N_4NdO_3$: C, 34.82; H, 3.34; N, 7.73. Found: C, 34.47; H, 3.22; N, 6.98. ^{1}H NMR (500 MHz, C_6D_6): δ 0.03 ppm (br s, 9 H, CH_3), 1.92 ppm (br s, 3 H, CH_2), 2.82 ppm (br s, 3 H, CH_2), 4.73 (br s, 3 H, CH), 5.22 ppm (br s, 3 H, CH_2), 6.49 ppm (br s, 3 H, CH_2). ^{19}F NMR (470 MHz, C_6D_6): δ −76.41 ppm (s). IR (cm^{-1}) 2949 (w), 2892 (w), 1480 (w), 1446 (w), 1426 (w), 1361 (m), 1307 (w), 1285 (m), 1268 (m), 1246 (s), 1223 (m), 1197 (w), 1150 (m), 1134 (s), 1098 (s), 1085 (s), 1050 (s), 1010 (s), 945 (s), 932 (m), 914 (m), 887 (m), 816 (s), 804 (m), 770 (s), 748 (w), 647 (s), 635 (s).

Computational details

While lattice energies can be determined in a more rigorous way using periodic density functional theory (DFT) methods, we hypothesized that a simple lattice model could explain the differences in volatility. Specifically, the number and specific type of contacts (interactions with the nearest neighbor) surrounding a monomer were analyzed by computing the non-covalent interactions (NCI) of the unit cell. The total interaction in the cell can be approximated as a sum of these pair-wise nearest neighbor interaction energies. Therefore, to analyze non-covalent interactions for each crystal, all possible dimers whose Yb–Yb distance is no longer than 11 Å were located. To account for every possible dimer, a supercell of 2 × 2 × 2 was considered. Subsequently, the positions of the hydrogen atoms were optimized at the PBE0-D3/def2-TZVP level of theory.[32–35] Heavy atoms were fixed at the experimental positions to ensure the solid-state environment was maintained. The obtained electron density was then used to calculate the NCIs. The identification and strength of the interactions were estimated using the IGMPlot software.[36–40]

Data availability

A data set collection of computational results is available in the ioChem-BD repository[41] and can be accessed online using the following link: **https://iochem-bd.bsc.es/browse/review-collection/100/314943/93ff121cbebcd98b8a00e40f**.

Conflicts of interest

There are no conflicts to declare.

Acknowledgements

References

1 A. Drozdov and N. Kuzmina, Volatile compounds of lanthanides, *Compr. Inorg. Chem. II*, 2013, **2**, 511–534.

2 A. F. Novgorodov, F. Rösch and N. A. Korolev, Radiochemical Separations by Thermochromatography, in *Handbook of Nuclear Chemistry*, ed. A. Vértes, S. Nagy, Z. Klencsár, R. G. Lovas and F. Rösch, Springer US, 2011, pp. 2429–2458.

3 I. Zvara, The fundamentals of vacuum thermochromatography, *J. Radioanal. Nucl. Chem.*, 2010, **286**, 597–602.

4 D. E. Hanson, J. R. Garrison and H. L. Hall, Assessing thermo chromatography as a separation method for nuclear forensics: current capability vis-a-vis forensic requirements, *J. Radioanal. Nucl. Chem.*, 2011, **289**, 213–223.

5 R. E. Sievers, K. J. Eisentraut, C. S. Springer Jr. and D. W. Meek, Volatile rare earth chelates of β-diketones, *Adv. Chem. Ser.*, 1967, **71**, 141–154.

6 J. A. Belot, A. Wang, R. J. McNeely, L. Liable-Sands, A. L. Rheingold and T. J. Marks, Highly volatile, low melting, fluorine-free precursors for metal-organic chemical vapor deposition of lanthanide oxide-containing thin films, *Chem. Vap. Deposition*, 1999, **5**, 65–69.

7 N. L. Edleman, A. Wang, J. A. Belot, A. W. Metz, J. R. Babcock, A. M. Kawaoka, J. Ni, M. V. Metz, C. J. Flaschenriem, C. L. Stern, L. M. Liable-Sands,

A. L. Rheingold, P. R. Markworth, R. P. H. Chang, M. P. Chudzik, C. R. Kannewurf and T. J. Marks, Synthesis and characterization of volatile, fluorine-free β-ketoiminate lanthanide MOCVD precursors and their implementation in low-temperature growth of epitaxial CeO$_2$ buffer layers for superconducting electronics, *Inorg. Chem.*, 2002, **41**, 5005–5023.

8 S. Battiato, P. Rossi, P. Paoli and G. Malandrino, Heterobimetallic Sodium Rare-Earth Complexes: "Third-Generation" MOCVD Precursors for the Deposition of NaREF$_4$ (RE = Y, Gd) Films, *Inorg. Chem.*, 2018, **57**, 15035–15039.

9 K. J. Eisentraut and R. E. Sievers, Thermogravimetric studies of metal β-diketonates, *J. Inorg. Nucl. Chem.*, 1967, **29**, 1931–1936.

10 C. S. Springer Jr., D. W. Meek and R. E. Sievers, Rare earth chelates of 1,1,1,2,2,3,3-heptafluoro-7,7-dimethyl-4,6-octanedione, *Inorg. Chem.*, 1967, **6**, 1105–1110.

11 J. E. Sicre, J. T. Dubois, K. J. Eisentraut and R. E. Sievers, Volatile lanthanide chelates. II. Vapor pressures, heats of vaporization, and heats of sublimation, *J. Am. Chem. Soc.*, 1969, **91**, 3476–3481.

12 K. Utsunomiya, Gas chromatography of rare-earth chelates of isobutyrylpivalylmethane, *Anal. Chim. Acta*, 1972, **59**, 147–151.

13 D. C. Bradley, J. S. Ghotra and F. A. Hart, Low coordination numbers in lanthanide and actinide compounds. I. Preparation and characterization of tris[bis(trimethylsilyl)amido]lanthanides, *J. Chem. Soc., Dalton Trans.*, 1973, 1021–1023.

14 J. M. Birmingham and G. Wilkinson, Cyclopentadienides of scandium, yttrium, and some rare earth elements, *J. Am. Chem. Soc.*, 1956, **78**, 42–44.

15 S. R. Daly, D. Y. Kim, Y. Yang, J. R. Abelson and G. S. Girolami, Lanthanide, *N,N*-dimethyl-aminodiboranates: highly volatile precursors for the deposition of lanthanide-containing thin films, *J. Am. Chem. Soc.*, 2010, **132**, 2106–2107.

16 S. R. Daly, D. Y. Kim and G. S. Girolami, Lanthanide, *N,N*-dimethylaminodiboranates as a new class of highly volatile chemical vapor deposition precursors, *Inorg. Chem.*, 2012, **51**, 7050–7065.

17 A. E. Khochenkov, N. V. Belova, A. V. Krasnov, Y. A. Zhabanov, N. I. Giricheva and G. V. Girichev, Sublimation enthalpy of tetrakis(1,1,1,5,5,5-hexafluoro-2,4-pentanedionato)lanthanide(III)-potassium complexes, KLn(C$_5$HF$_6$O$_2$)$_4$: Effect of lanthanide contraction, *J. Chem. Thermodyn.*, 2019, **131**, 117–121.

18 A. S. Hyre and L. H. Doerrer, A structural and spectroscopic overview of molecular lanthanide complexes with fluorinated O-donor ligands, *Coord. Chem. Rev.*, 2020, **404**, 213098.

19 E. W. Berg and J. J. Chiang-Acosta, Fractional sublimation of the β-diketone chelates of the lanthanide and related elements, *Anal. Chim. Acta*, 1968, **40**, 101–113.

20 J. Schläfer, D. Graf, G. Fornalczyk, A. Mettenbörger and S. Mathur, Fluorinated Cerium(IV) Enaminolates: Alternative

Precursors for Chemical Vapor Deposition of CeO$_2$ Thin Films, *Inorg. Chem.*, 2016, **55**, 5422–5429.

21 D. J. Berg, S. J. Rettig and C. Orvig, Heptadentate ligands for the lanthanides. The first structurally characterized example of a lanthanide heptadentate ligand complex: [tris(3-aza-4-methyl-6-oxohept-4-en-1-yl)amine]ytterbium(III), *J. Am. Chem. Soc.*, 1991, **113**, 2528–2532.

22 A. Smith, S. J. Rettig and C. Orvig, Lanthanide complexes of potentially heptadentate ligands including the structure of [tris(3-aza-4-methylhept-4-ene-6-on-1-yl)amine]tris(nitrato)gadolinium(III), *Inorg. Chem.*, 1988, **27**, 3929–3934.

23 R. Hoffmann, B. F. Beier, E. L. Muetterties and A. R. Rossi, Seven-coordination. A molecular orbital exploration of structure, stereochemistry, and reaction dynamics, *Inorg. Chem.*, 1977, **16**, 511–522.

24 W. S. Rees Jr., O. Just, S. L. Castro and J. S. Matthews, Synthesis and magnetic and structural characterization of the first homoleptic lanthanide β-ketoiminate, *Inorg. Chem.*, 2000, **39**, 3736–3737.

25 Q. Xia, Y. Cui, D. Yuan, Y. Wang and Y. Yao, Synthesis and characterization of lanthanide complexes stabilized by N-aryl substituted β-ketoiminato ligands and their application in the polymerization of rac-lactide, *J. Organomet. Chem.*, 2017, **846**, 161–168.

26 R. D. Shannon, Revised effective ionic radii and systematic studies of interatomic distances in halides and chalcogenides, *Acta Crystallogr., Sect. A: Cryst. Phys., Diffr., Theor. Gen. Crystallogr.*, 1976, **32**, 751–767.

27 S. M. Cohen, M. Meyer and K. N. Raymond, Enterobactin Protonation and Iron Release: Hexadentate Tris-Salicylate Ligands as Models for Triprotonated Ferric Enterobactin, *J. Am. Chem. Soc.*, 1998, **120**, 6277–6286.

28 S. M. Cohen and K. N. Raymond, Catecholate/Salicylate Heteropodands: Demonstration of a Catecholate to Salicylate Coordination Change[1], *Inorg. Chem.*, 2000, **39**, 3624–3631.

29 T. Müntener, D. Joss, D. Häussinger and S. Hiller, Pseudocontact Shifts in Biomolecular NMR Spectroscopy, *Chem. Rev.*, 2022, **122**, 9422–9467.

30 K. Mason, A. C. Harnden, C. W. Patrick, A. W. J. Poh, A. S. Batsanov, E. A. Suturina, M. Vonci, E. J. L. McInnes, N. F. Chilton and D. Parker, Exquisite sensitivity of the ligand field to solvation and donor polarisability in coordinatively saturated lanthanide complexes, *Chem. Commun.*, 2018, **54**, 8486–8489.

31 D. C. Bradley, J. S. Ghotra and F. A. Hart, Three coordination in lanthanide chemistry: tris[bis(trimethylsilyl)amido]lanthanide(III) compounds, *J. Chem. Soc., Chem. Commun.*, 1972, 349–350.

32 C. Adamo and V. Barone, Toward reliable density functional methods without adjustable parameters: The PBE0 model, *J. Chem. Phys.*, 1999, **110**, 6158–6170.

33 S. Grimme, J. Antony, S. Ehrlich and H. Krieg, A consistent and accurate ab initio parametrization of density functional dispersion correction (DFT-D) for the 94 elements H-Pu, *J. Chem. Phys.*, 2010, **132**, 154104.

34 F. Weigend and R. Ahlrichs, Balanced basis sets of split valence, triple zeta valence and quadruple zeta valence quality for H to Rn: Design and assessment of accuracy, *Phys. Chem. Chem. Phys.*, 2005, **7**, 3297–3305.

35 F. Weigend, Accurate Coulomb-fitting basis sets for H to Rn, *Phys. Chem. Chem. Phys.*, 2006, **8**, 1057–1065.

36 C. Lefebvre, G. Rubez, H. Khartabil, J.-C. Boisson, J. Contreras-García and E. Hénon, Accurately extracting the signature of intermolecular interactions present in the NCI plot of the reduced density gradient versus electron density, *Phys. Chem. Chem. Phys.*, 2017, **19**, 17928–17936.

37 C. Lefebvre, H. Khartabil, J.-C. Boisson, J. Contreras-García, J.-P. Piquemal and E. Hénon, The Independent Gradient Model: A New Approach for Probing Strong and Weak Interactions in Molecules from Wave Function Calculations, *ChemPhysChem*, 2018, **19**, 724–735.

38 J. Klein, H. Khartabil, J.-C. Boisson, J. Contreras-García, J.-P. Piquemal and E. Hénon, New Way for Probing Bond Strength, *J. Phys. Chem. A*, 2020, **124**, 1850–1860.

39 M. Ponce-Vargas, C. Lefebvre, J.-C. Boisson and E. Hénon, Atomic Decomposition Scheme of Noncovalent Interactions Applied to Host–Guest Assemblies, *J. Chem. Inf. Model.*, 2020, **60**, 268–278.

40 C. Lefebvre, J. Klein, H. Khartabil, J. C. Boisson and E. Hénon, IGMPlot: A program to identify, characterize, and quantify molecular interactions, *J. Comput. Chem.*, 2023, **44**, 1750–1766.

41 M. Álvarez-Moreno, C. de Graaf, N. López, F. Maseras, J. M. Poblet and C. Bo, Managing the Computational Chemistry Big Data Problem: The ioChem-BD Platform, *J. Chem. Inf. Model.*, 2015, **55**, 95–103.